Article

Widespread phytoplankton blooms triggered by 2019–2020 Australian wildfires

Weiyi Tang[1,11,12], Joan Llort[2,3,12], Jakob Weis[2,4], Morgane M. G. Perron[2], Sara Basart[3], Zuchuan Li[1,5], Shubha Sathyendranath[6], Thomas Jackson[6], Estrella Sanz Rodriguez[7], Bernadette C. Proemse[2], Andrew R. Bowie[2,8], Christina Schallenberg[2,8], Peter G. Strutton[2,4], Richard Matear[9 ✉] & Nicolas Cassar[1,10 ✉]

Droughts and climate-change-driven warming are leading to more frequent and intense wildfires[1–3], arguably contributing to the severe 2019–2020 Australian wildfires[4]. The environmental and ecological impacts of the fires include loss of habitats and the emission of substantial amounts of atmospheric aerosols[5–7]. Aerosol emissions from wildfires can lead to the atmospheric transport of macronutrients and bio-essential trace metals such as nitrogen and iron, respectively[8–10]. It has been suggested that the oceanic deposition of wildfire aerosols can relieve nutrient limitations and, consequently, enhance marine productivity[11,12], but direct observations are lacking. Here we use satellite and autonomous biogeochemical Argo float data to evaluate the effect of 2019–2020 Australian wildfire aerosol deposition on phytoplankton productivity. We find anomalously widespread phytoplankton blooms from December 2019 to March 2020 in the Southern Ocean downwind of Australia. Aerosol samples originating from the Australian wildfires contained a high iron content and atmospheric trajectories show that these aerosols were likely to be transported to the bloom regions, suggesting that the blooms resulted from the fertilization of the iron-limited waters of the Southern Ocean. Climate models project more frequent and severe wildfires in many regions[1–3]. A greater appreciation of the links between wildfires, pyrogenic aerosols[13], nutrient cycling and marine photosynthesis could improve our understanding of the contemporary and glacial–interglacial cycling of atmospheric CO_2 and the global climate system.

Human activity is altering the global water and carbon cycles[14]. While the risk of drought associated with climate change varies regionally, warming and drying will increase the risk of more frequent and intense wildfires[1–3]. In turn, wildfires are increasingly viewed as a first-order control on climate. Among other things, wildfires change the Earth's radiative forcing by emitting greenhouse gases and aerosols[15]. The feedbacks between climate and wildfires are complex and often poorly represented in climate models, leading to high uncertainty in future projections.

The austral summer of 2019–2020 was one of the most severe wildfire seasons in Australian history. Millions of hectares of vegetation were burned, having ecological, environmental and socioeconomical impacts[5,16]. It is estimated that nearly 3 billion animals may have died or been displaced[17]. According to a study by van der Velde et al. published in this issue of *Nature*[18], approximately 715 million tonnes of CO_2 (195 Tg C) were released into the atmosphere during the fire period, exceeding Australia's 2018 anthropogenic CO_2 emissions of 537.4 million tonnes (147 Tg C)[19].

The 2019–2020 Australian wildfires (known in Australia as bushfires) also released an enormous amount of aerosols into the atmosphere[6,7]. Aerosols can influence terrestrial and marine biogeochemistry[20], via supplying soluble forms of nitrogen[8], phosphorus[9], and bio-essential trace metals including iron (Fe)[10,13]. The high-nutrient low-chlorophyll (HNLC) waters of the Southern Ocean are mostly iron-limited[21]. Delivery of Fe to these waters is believed to be an essential driver of oceanic primary production, atmospheric CO_2 uptake by the oceans, and to modify climate over geological timescales[22,23]. In the open waters of the Southern Ocean, the dominant Fe sources are deep winter mixing[24], dust[25,26], hydrothermalism[27], and ice melt[28].

Here we provide a first assessment of how the 2019–2020 Australian wildfires stimulated an expansive phytoplankton response in the Southern Ocean. While the impact of wildfires on local terrestrial nutrient dynamics through soil erosion and aerosol deposition is well studied[29], our work demonstrates the potential of wildfires to impact marine ecosystems thousands of kilometres away through long-range atmospheric aerosol transport. During the 2019–2020 Australian

[1]Division of Earth and Climate Sciences, Nicholas School of the Environment, Duke University, Durham, NC, USA. [2]Institute for Marine and Antarctic Studies, University of Tasmania, Hobart, Tasmania, Australia. [3]Barcelona Supercomputing Centre, Barcelona, Spain. [4]Australian Research Council Centre of Excellence for Climate Extremes, University of Tasmania, Hobart, Tasmania, Australia. [5]Applied Ocean Physics and Engineering, Woods Hole Oceanographic Institution, Woods Hole, MA, USA. [6]Plymouth Marine Laboratory, Plymouth, UK. [7]Australian Centre for Research on Separation Science (ACROSS), School of Natural Sciences, University of Tasmania, Hobart, Tasmania, Australia. [8]Australian Antarctic Program Partnership, University of Tasmania, Hobart, Tasmania, Australia. [9]CSIRO Oceans and Atmosphere, Hobart, Tasmania, Australia. [10]CNRS, Univ Brest, IRD, Ifremer, LEMAR, Plouzané, France. [11]Present address: Department of Geosciences, Princeton University, Princeton, NJ, USA. [12]These authors contributed equally: Weiyi Tang, Joan Llort. ✉e-mail: richard.matear@csiro.au; nicolas.cassar@duke.edu
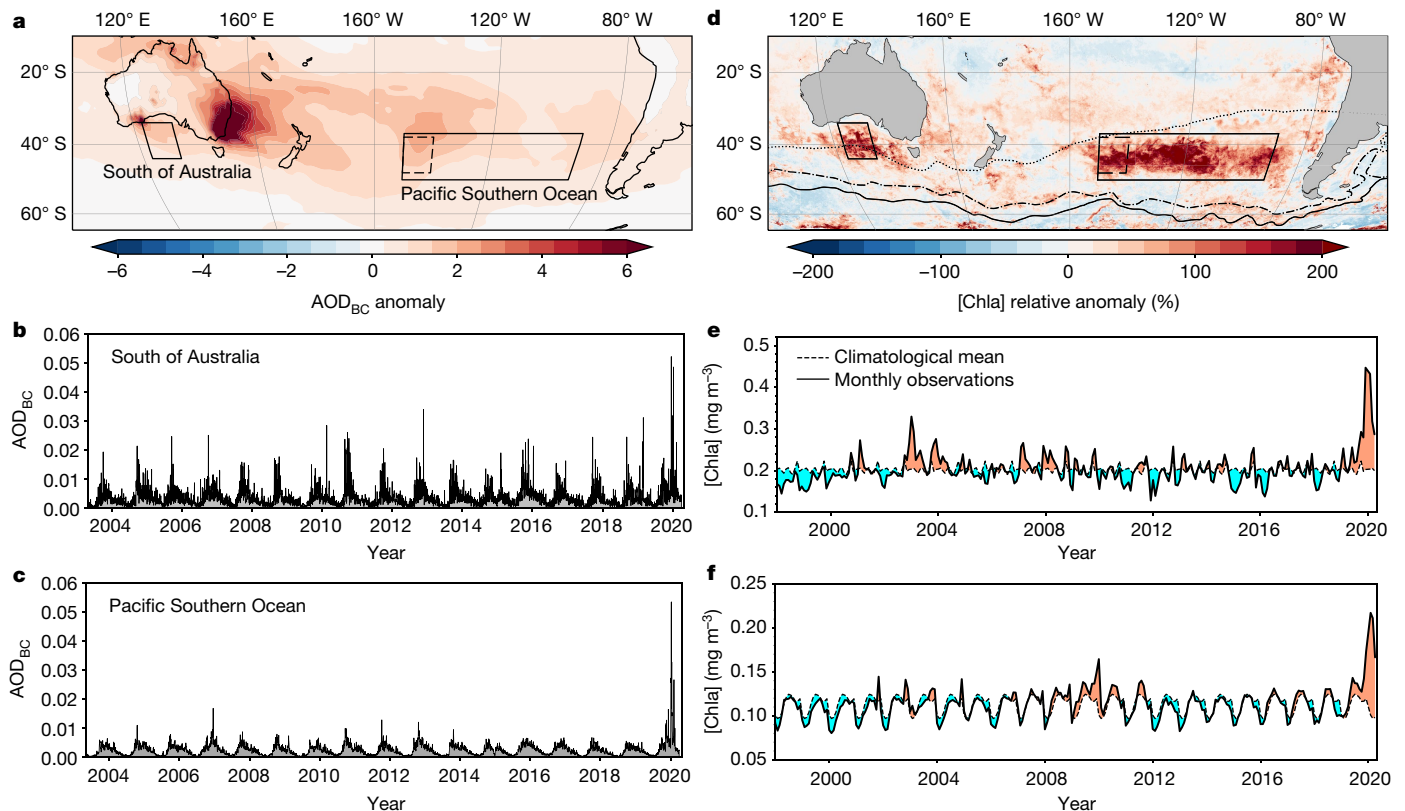
Fig. 1 | Maps of black carbon AOD and [Chla] anomalies and their historical records. a, Cumulative black carbon AOD (AOD$_{BC}$) anomaly for the 2019–2020 austral summer. **b**, Daily time-series of black carbon AOD for waters south of Australia (solid black box in panels **a** and **d**). **c**, Daily time-series of black carbon AOD in the Pacific Southern Ocean (solid black box in panels **a** and **d**). **d**, [Chla] relative anomaly for the 2019–2020 austral summer. The dashed box within the 'Pacific Southern Ocean' box is used to show temporal variations of black carbon AOD and [Chla] time-series during the 2019–2020 Australian wildfires

in Fig. 2. **e**, Monthly time-series of [Chla] in waters south of Australia (solid black line). Monthly climatological values are shown with a dotted black line. Red and cyan areas denote monthly data higher or lower than climatological values, respectively. **f**, Monthly time-series of [Chla] in the Pacific subantarctic Southern Ocean (south of the Subtropical Front). Dotted, dot-dashed and solid black lines in **d** represent the climatological positions of the Subtropical Front, Subantarctic Front and Polar Front, respectively[48].

wildfires, vast aerosol plumes from biomass burning were emitted into the atmosphere from southern and eastern Australia, as revealed by Moderate Resolution Imaging Spectroradiometer (MODIS) satellite aerosol retrievals (Extended Data Fig. 1a). Some aerosols and gases reached altitudes of up to 16 km, causing previously undocumented changes in stratospheric winds[6] and further highlighting the intensity and uniqueness of the 2019–2020 Australian wildfires. Since aerosol optical depth (AOD) in the visible spectral range (at 550 nm) reflects bulk aerosol load in the atmospheric column, including desert dust, sea salt, sulfate, organic matter and black carbon, we use black carbon AOD estimated by the Copernicus Atmosphere Monitoring Service (CAMS) reanalysis[30] as a proxy for wildfire aerosols (see Methods).

Black carbon AOD shows that wildfire emissions emanated mainly from southern and eastern Australia and extended within a few days to the broad South Pacific between 20° S and 55° S (Fig. 1a, Extended Data Fig. 1 and Supplementary Video). Predominantly eastward aerosol transport is confirmed by air parcel forward trajectories initiated at the locations of wildfires (Extended Data Fig. 2). Emissions of black carbon aerosols were episodic. For example, the signal from 8 January 2020 alone accounted for ~25% of the cumulative black carbon AOD for the whole month of January 2020. As AOD does not necessarily translate into deposition, we used the deposition fluxes estimated in the CAMS reanalysis and satellite chlorophyll a concentration ([Chla]) anomalies to define the oceanic regions with potential phytoplankton fertilization by aerosols from 2019–2020 Australian wildfires (see Methods for the model estimate of aerosol deposition and satellite [Chla] observations). By December 2019, [Chla] had increased by over 150% compared with

monthly climatologies in large areas of the ocean. The surface area of the regions with [Chla] higher than the historical monthly maximum (>10 trillion m^2) exceeded the size of Australia (Fig. 1d). We identified two regions, south of Australia and Pacific sector of the Southern Ocean, where [Chla] more than doubled compared with the climatological concentrations and atmospheric deposition exceeded 150 mg m^{-2} in the 2019–2020 austral summer (Extended Data Fig. 3). In these two study regions (Fig. 1a, d), black carbon AOD reached values unprecedented in the 17-year aerosol reanalysis time series (at least 300% higher than their climatological values shown in Fig. 1b, c) and [Chla] reached concentrations never observed in a 22-year satellite time-series from the European Space Agency's Ocean Colour Climate Change Initiative (OC-CCI) (Fig. 1e, f). While the forward air-parcel trajectories show that the high [Chla] anomaly regions are in the path of the pyrogenic aerosol transport (Extended Data Fig. 2), we applied two different approaches to demonstrate the unprecedented nature of the [Chla] anomaly. First, we assessed the basin-wide response of [Chla] to the black carbon AOD anomaly (Extended Data Fig. 4), and second, we iteratively analysed 4,681 different 10 × 10 degree geographical domains in the South Pacific and Pacific sector of the Southern Ocean over the entire remotely sensed ocean colour record (Extended Data Fig. 5). These analyses show that the [Chla] anomaly during the 2019–2020 Australian wildfires is unprecedented in the satellite record independently of how we define the study regions.

The [Chla] anomalies followed peaks in black carbon AOD with lag times on the order of days to weeks (Fig. 2). Earlier studies have explored the potential for dust to stimulate phytoplankton blooms and found
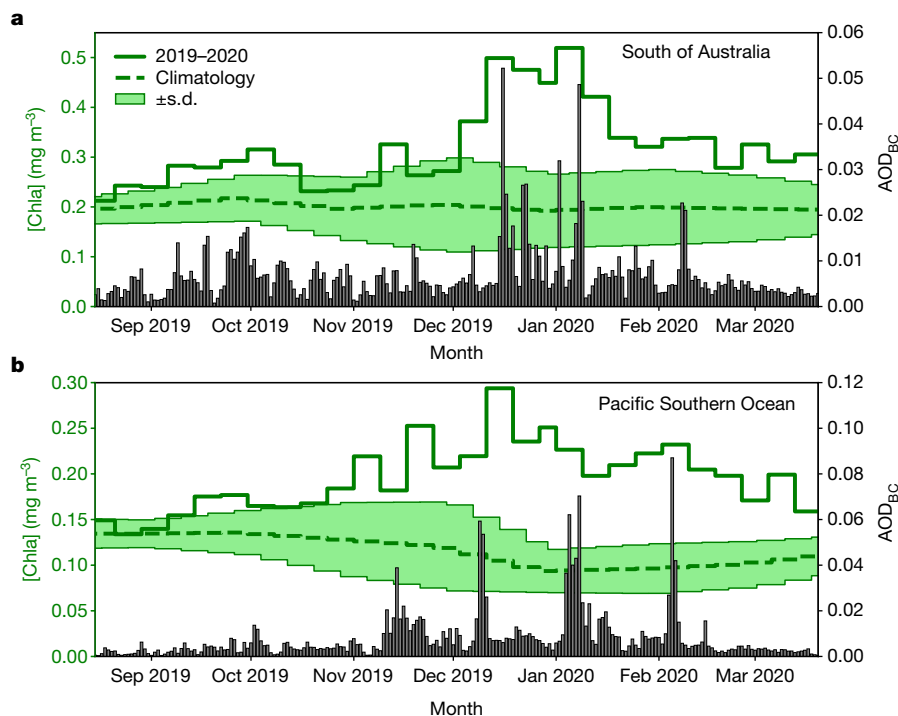
Fig. 2 | Temporal patterns of black carbon AOD and satellite [Chla] in two regions denoted in Fig. 1 during the 2019–2020 Australian wildfire season. a, **b**, Waters south of Australia (**a**) and Pacific Southern Ocean (south of the Subtropical Front) (**b**). Daily black carbon AOD is shown in vertical bars. Solid and dashed green lines represent the 8-day mean [Chla] for 2019–2020 and climatological records, respectively. Green shaded areas indicate ±1 standard deviation. The episodic aerosol transport events are illustrated by the sharp peaks of black carbon AOD while the biological responses are sustained for a longer period.

similar relations between [Chla] and AOD[26,31]. The anomalous phytoplankton blooms started around October 2019, peaked in January 2020 and lasted for over 4 months with regional differences (Fig. 2). The plankton blooms were independently confirmed by contemporaneous in situ measurements of particle concentrations from optical backscattering on biogeochemical (BGC) Argo floats, showing particle concentrations well above a climatology envelope during the bloom period (Fig. 3 and Extended Data Fig. 6, see Methods for BGC-Argo float measurements). Furthermore, [Chla] measured by the BGC-Argo floats confirmed that the observed particles were phytoplankton (Fig. 3), ruling out potential contamination of optical backscattering by aerosols (Supplementary Discussion). Most surprising is that the phytoplankton increase occurred in austral summer when a seasonal decline in [Chla] is normally observed (Fig. 1 and Extended Data Fig. 4). In these regions of the Southern Ocean, photosynthesis is generally limited by Fe in austral summer when light is sufficient and mixed layers are often shallower than 45 m (refs. [21,32,33]). Therefore, additional Fe supply is required to support these anomalous phytoplankton blooms.

To evaluate the fertilization potential of the 2019–2020 Australian wildfire aerosols, we tracked wildfire emissions and transport in the atmosphere and measured Fe concentration in aerosols collected at a time-series station on the island of Tasmania, mostly downwind from the fire events in mainland Australia (see Methods). The total and labile concentrations of Fe (T_{Fe} and L_{Fe}) were substantially higher in fire-sourced samples than in historical values (Extended Data Fig. 7). The highest total and labile concentrations of Fe (T_{Fe} = 257.4 ng m^{-3} and L_{Fe} = 73.9 ng m^{-3}) were measured in aerosols between 15 and 17 January 2020. This sample also contained the highest concentration of levoglucosan (indicating the presence of biomass-burning emissions in aerosols) and was collected while a large black carbon AOD plume travelled over the sampling location (Extended Data Fig. 8). Air parcel back trajectories confirm that the black carbon AOD plume originated from southeast Australia, the epicentre of the 2019–2020 Australian

megafires (Extended Data Fig. 8). Wildfire-impacted aerosols showed significantly higher T_{Fe} ($p < 0.05$, up to fivefold increase) and L_{Fe} ($p < 0.1$, up to 27-fold increase) concentrations than measurements at the same station between 2016 and 2019 (all seasons), including smaller and more localized wildfire events. This observation is consistent with other studies showing large atmospheric Fe input from pyrogenic sources[13]. The fraction of labile Fe was likely to be greater over our study region of the Pacific sector of the Southern Ocean as solubility is known to increase during atmospheric transport[34]. Preliminary estimates show that Fe supply from aerosol deposition is sufficient to fulfill the Fe requirement to support the anomalous [Chla] increase (Supplementary Discussion). While Fe could have been supplied by other sources such as vertical mixing of Fe-rich water[35], we did not find a strong negative correlation between sea surface temperature and [Chla] anomalies in our study region and period (Supplementary Fig. 7). Overall, our analyses suggest that Fe-rich aerosols emanating from the 2019–2020 Australian wildfires were capable of fertilizing the observed expansive algal blooms in the Southern Ocean. While our study focuses on Fe, pyrogenic aerosols may also have contributed nutrients other than Fe[8,9], jointly stimulating phytoplankton response in the broad areas covered by elevated AOD plume (Fig. 1).

We evaluated the anomalous carbon export associated with phytoplankton blooms. Since AOD (and aerosol deposition) and phytoplankton productivity were enhanced in a larger portion of the South Pacific and Southern Ocean than the two selected regions in Fig. 1, we define a basin scale region of interest as the region with positive black carbon AOD anomalies (Extended Data Fig. 9). Satellite-estimated marine net primary production (NPP) and export production (EP) increased substantially during the 2019–2020 Australian wildfire season compared with the monthly climatologies (Fig. 4), corresponding to a cumulative net additional uptake of ~186 ± 90 Tg C from October 2019 to April 2020, equivalent to ~95 ± 46% of the CO_2 emission (~195 Tg C) from the 2019–2020 Australian wildfires. We refrain from
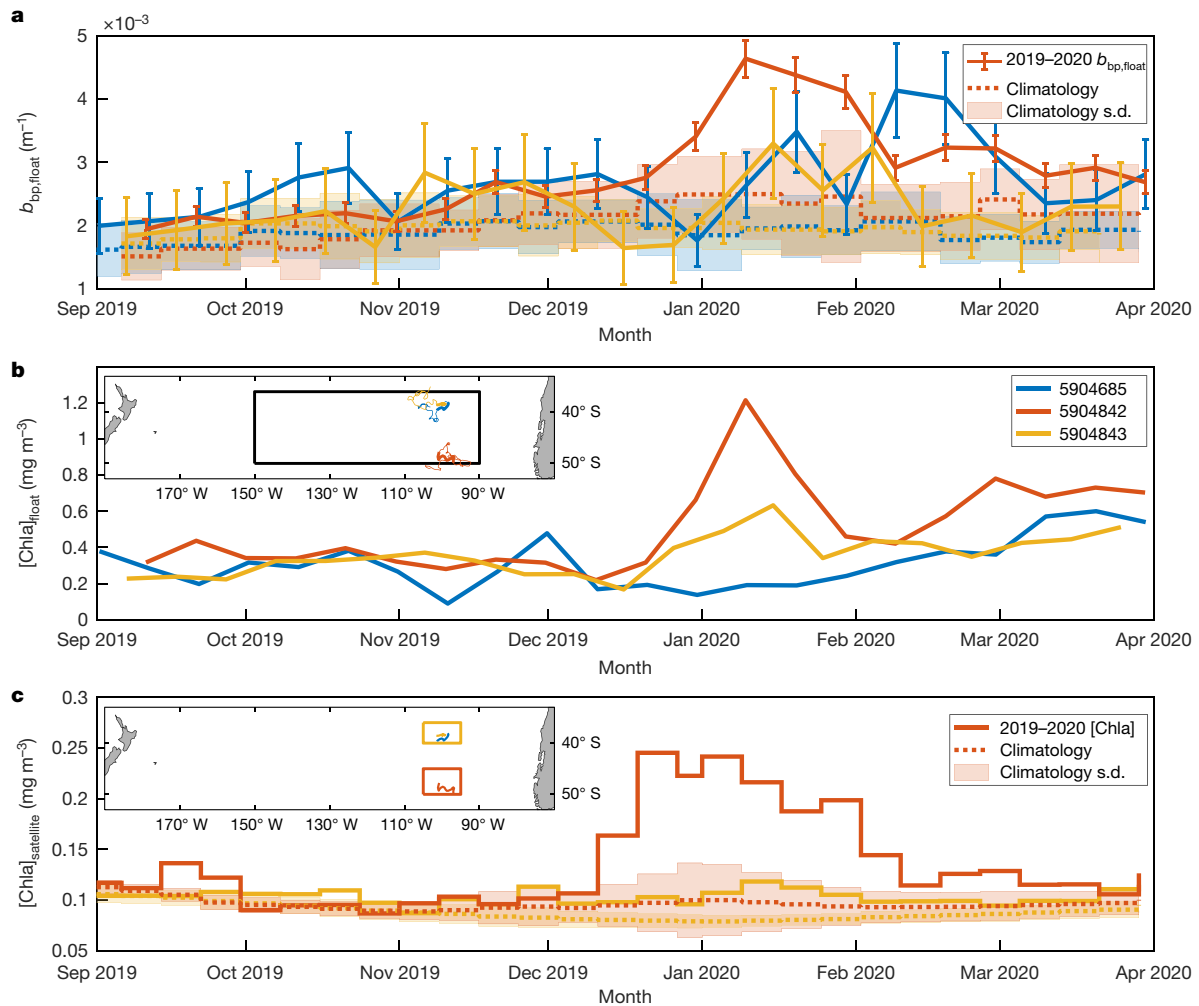
Fig. 3 | Plankton blooms observed by in situ measurements from BGC-Argo floats and satellites. a, Comparison between in situ summer 2019–2020 particulate backscatter (b_{bp}, solid lines) measured by three BGC-Argo floats and the corresponding satellite climatology (dotted lines, standard deviation shown as envelope). Float trajectories are displayed on the inset map in subplot **b** (line and trajectory colours correspond). Float b_{bp} was calibrated to satellite b_{bp} (see Methods for details). Error bars indicate the uncertainty introduced by the calibration. Climatological b_{bp} values were calculated individually from satellite b_{bp} for each profile location. **b**, In situ [Chla] measured by the three BGC-Argo floats. Float positions from September 2019 through March 2020 are highlighted (traveling mostly from west to east during the fire season). Float IDs are specified in the key. **c**, Satellite [Chla] average over two sub-regions encompassing the float paths.

providing an air–sea CO_2 flux associated with the anomalous carbon export because the ratio of cumulative air–sea CO_2 flux to carbon export associated with Fe fertilization varies as a function of numerous factors and is highly uncertain[36] (Supplementary Discussion). We also note that the additional CO_2 uptake may not have been exported to the deep ocean, in which case the sequestration may be short-lived[21]. In addition, the responding phytoplankton groups remain to be determined, which could affect the carbon export efficiency. For example, the low silicic acid concentration in parts of the subantarctic zone may restrict the response of diatoms to Fe fertilization[37]. The large-scale and long-term effects of the 2019–2020 Australian wildfires on primary production, carbon export and CO_2 exchange warrant further study.

Large-scale climate patterns influence ocean dynamics, nutrient supply and light regime, thereby modulating productivity and carbon uptake in the Southern Ocean[38]. While the El Niño–Southern Oscillation (ENSO) index was neutral during the 2019–2020 Australian wildfires, the Indian Ocean Dipole (IOD) and Southern Annular Mode (SAM) were strongly positive and negative, respectively (Extended Data Fig. 10). However, [Chla] anomalies potentially driven by climate modes are substantially smaller (<10%) than what we observed during

the 2019–2020 Australian wildfire season, as demonstrated by the predicted magnitude of the 2019–2020 excursion from the climatologies (Extended Data Fig. 10d, e). Climate patterns could also set the stage for conditions favourable to wildfires[39,40]. Positive IOD and negative SAM are believed to precondition southeast Australia for wildfires by reducing rainfall and increasing temperature[4,39]. Perhaps more importantly, the 2019–2020 summer in southeast Australia was also strongly driven towards hot and dry conditions by a stratospheric warming event[41]. Some Australian megafires have occurred during positive IOD and/or negative SAM events in the historical record (Extended Data Fig. 10). The frequency of extreme positive IOD is predicted to increase due to global warming, rendering southeastern Australia and eastern Asia more susceptible to wildfires[42]. The impact on marine ecosystems downwind of these wildfires is likely to depend on the wildfire intensity and duration, dispersal of pyrogenic aerosols, seasonal timing, and the ecosystem's initial state. A plankton ecosystem may not be responsive to Fe-rich aerosol deposition because of macronutrient or light limitation[43]. Some of these factors may explain why not all Australian wildfires on record are associated with marine biological responses (Fig. 1 and Extended Data Fig. 10). Macronutrient limitation could also explain the lack of a strong [Chla] response in oligotrophic subtropical waters
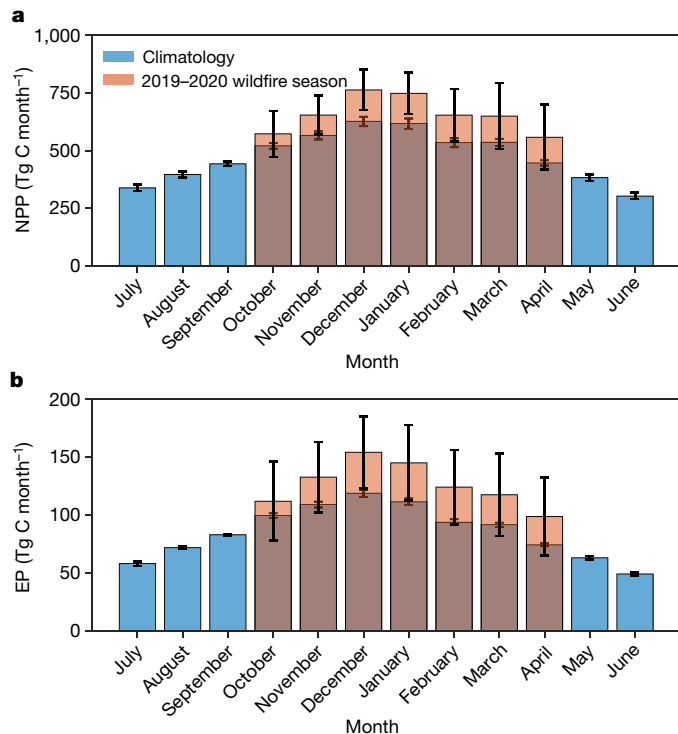
Fig. 4 | Enhancement in marine phytoplankton productivity during the 2019–2020 Australian wildfires. a, b, Satellite-estimated monthly net primary production (NPP) (**a**) and export production (EP) (**b**) during 2019–2020 Australian wildfire season (orange bars) compared with their monthly climatologies (blue bars) at the basin scale (20° S–55° S, 120° E–90° W) (Extended Data Fig. 9). Error bars represent one standard deviation of monthly NPP or EP from 2003 to 2018 (for climatology) and from October 2019 to April 2020 (for wildfire season) derived from three NPP and nine EP model estimates. The total anomalous NPP and EP were 753 ± 300 Tg C and 186 ± 90 Tg C, respectively, from October 2019 to April 2020.

east of Australia despite being overlain with high black carbon AOD and aerosol deposition during the 2019–2020 Australian wildfires (Supplementary Discussion).

Modelling studies have highlighted the potential role of fire in providing bioavailable Fe and other nutrients to downwind regions through atmospheric transport[11,44]. Building on these studies, we provide observational evidence that aerosols originating from megafires contain sufficient Fe to support a large phytoplankton response in the ocean. Human activity has altered nutrient supply and deposition to the ocean through local and global perturbations. Local perturbations such as land use change and fossil fuel burning enhance micronutrient and macronutrient mobilization and emission to the atmosphere[44,45]. In turn, global perturbations to the water cycle and heat budget are leading to changes in wildfire and drought distributions, frequency and intensity[14]. There is increasing evidence that wildfires may have had an important role modulating atmospheric CO_2 during glacial–interglacial periods[46]. They currently burn approximately 3% of the Earth's land annually, in the process emitting ~2.2 Pg C yr^{-1} (ref. [47]). Given the increasing risk of wildfires with climate change (for example, in southeast Australia, the Amazon, and the western United States)[1–3], their central role in our global climate in the geological past, at present, and in our future therefore argues for a more comprehensive representation of wildfires in climate models. Among other things, extensive measurements of wildfire aerosols and targeted studies of their effects on marine ecosystems are needed to further elucidate the wide-ranging impacts, especially for an event of the magnitude of the 2019–2020 Australian wildfires.

Online content

Any methods, additional references, Nature Research reporting summaries, source data, extended data, supplementary information, acknowledgements, peer review information; details of author contributions and competing interests; and statements of data and code availability are available at https://doi.org/10.1038/s41586-021-03805-8.

1. Bowman, D. M. J. S. et al. Vegetation fires in the Anthropocene. *Nat. Rev. Earth Environ.* **1**, 500–515 (2020).
2. Abatzoglou, J. T., Williams, A. P. & Barbero, R. Global emergence of anthropogenic climate change in fire weather indices. *Geophys. Res. Lett.* **46**, 326–336 (2019).
3. Huang, Y., Wu, S. & Kaplan, J. O. Sensitivity of global wildfire occurrences to various factors in the context of global change. *Atmos. Environ.* **121**, 86–92 (2015).
4. van Oldenborgh, G. J. et al. Attribution of the Australian bushfire risk to anthropogenic climate change. *Nat. Hazards Earth Syst. Sci.* **21**, 941–960 (2021).
5. Ward, M. et al. Impact of 2019–2020 mega-fires on Australian fauna habitat. *Nat. Ecol. Evol.* **4**, 1321–1326 (2020).
6. Kablick III, G. P., Allen, D. R., Fromm, M. D. & Nedoluha, G. E. Australian PyroCb smoke generates synoptic-scale stratospheric anticyclones. *Geophys. Res. Lett.* **47**, e2020GL088101 (2020).
7. Hirsch, E. & Koren, I. Record-breaking aerosol levels explained by smoke injection into the stratosphere. *Science* **371**, 1269–1274 (2021).
8. Schlosser, J. S. et al. Analysis of aerosol composition data for western United States wildfires between 2005 and 2015: Dust emissions, chloride depletion, and most enhanced aerosol constituents. *J. Geophys. Res. Atmos.* **122**, 8951–8966 (2017).
9. Barkley, A. E. et al. African biomass burning is a substantial source of phosphorus deposition to the Amazon, Tropical Atlantic Ocean, and Southern Ocean. *Proc. Natl Acad. Sci. USA* **116**, 16216–16221 (2019).
10. Guieu, C., Bonnet, S., Wagener, T. & Loÿe-Pilot, M.-D. Biomass burning as a source of dissolved iron to the open ocean? *Geophys. Res. Lett.* **32**, L19608 (2005).
11. Ito, A. Mega fire emissions in Siberia: potential supply of bioavailable iron from forests to the ocean. *Biogeosciences* **8**, 1679–1697 (2011).
12. Abram, N. J., Gagan, M. K., McCulloch, M. T., Chappell, J. & Hantoro, W. S. Coral reef death during the 1997 Indian Ocean Dipole linked to Indonesian wildfires. *Science* **301**, 952–955 (2003).
13. Ito, A. et al. Pyrogenic iron: the missing link to high iron solubility in aerosols. *Sci. Adv.* **5**, eaau7671 (2019).
14. Jia, G. et al. in *Climate Change and Land: an IPCC Special Report on Climate Change, Desertification, Land Degradation, Sustainable Land Management, Food Security, and Greenhouse Gas Fluxes in Terrestrial Ecosystems* Ch. 2 (IPCC, in the press).
15. Jiang, Y. et al. Impacts of wildfire aerosols on global energy budget and climate: the role of climate feedbacks. *J. Clim.* **33**, 3351–3366 (2020).
16. Bowman, D. et al. Wildfires: Australia needs national monitoring agency. *Nature* **584**, 188–191 (2020).
17. New WWF report: 3 billion animals impacted by Australia's bushfire crisis. *WWF* https://www.wwf.org.au/news/news/2020/3-billion-animals-impacted-by-australia-bushfire-crisis#gs.ebzve2 (2020).
18. van der Velde, I. R. et al. Vast CO_2 release from Australian fires in 2019–2020 constrained by satellite. *Nature* https://doi.org/10.1038/s41586-021-03712-y (2021).
19. *National Greenhouse Gas Inventory Report: 2018* (Australian Government, 2020); https://www.industry.gov.au/data-and-publications/national-greenhouse-gas-inventory-report-2018.
20. Mahowald, N. M. et al. Aerosol impacts on climate and biogeochemistry. *Annu. Rev. Environ. Res.* **36**, 45–74 (2011).
21. Boyd, P. W. et al. Mesoscale iron enrichment experiments 1993–2005: synthesis and future directions. *Science* **315**, 612–617 (2007).
22. Jickells, T. et al. Global iron connections between desert dust, ocean biogeochemistry, and climate. *Science* **308**, 67–71 (2005).
23. Martin, J. H. Glacial-interglacial CO_2 change: the iron hypothesis. *Paleoceanography* **5**, 1–13 (1990).
24. Tagliabue, A. et al. Surface-water iron supplies in the Southern Ocean sustained by deep winter mixing. *Nat. Geosci.* **7**, 314–320 (2014).
25. Cassar, N. et al. The Southern Ocean biological response to aeolian iron deposition. *Science* **317**, 1067–1070 (2007).
26. Gabric, A. J., Cropp, R., Ayers, G. P., McTainsh, G. & Braddock, R. Coupling between cycles of phytoplankton biomass and aerosol optical depth as derived from SeaWiFS time series in the Subantarctic Southern Ocean. *Geophys. Res. Lett.* **29**, 16-11–16-14 (2002).
27. Ardyna, M. et al. Hydrothermal vents trigger massive phytoplankton blooms in the Southern Ocean. *Nat. Commun.* **10**, 2451 (2019).
28. Duprat, L. P. A. M., Bigg, G. R. & Wilton, D. J. Enhanced Southern Ocean marine productivity due to fertilization by giant icebergs. *Nat. Geosci.* **9**, 219–221 (2016).
29. Bixby, R. J. et al. Fire effects on aquatic ecosystems: an assessment of the current state of the science. *Freshwater Sci.* **34**, 1340–1350 (2015).
30. Inness, A. et al. The CAMS reanalysis of atmospheric composition. *Atmos. Chem. Phys.* **19**, 3515–3556 (2019).
31. Shafeeque, M., Sathyendranath, S., George, G., Balchand, A. N. & Platt, T. Comparison of seasonal cycles of phytoplankton chlorophyll, aerosols, winds and sea-surface temperature off Somalia. *Front. Marine Sci.* **4**, 384 (2017).
32. Cassar, N. et al. The influence of iron and light on net community production in the Subantarctic and Polar Frontal zones. *Biogeosciences* **8**, 227–237 (2011).
33. Mitchell, B. G. & Holm-Hansen, O. Observations of modeling of the Antarctic phytoplankton crop in relation to mixing depth. *Deep Sea Res. Part A* **38**, 981–1007 (1991).

34. Longo, A. F. et al. Influence of atmospheric processes on the solubility and composition of iron in Saharan dust. *Environ. Sci. Technol.* **50**, 6912–6920 (2016).

35. Meskhidze, N., Nenes, A., Chameides, W. L., Luo, C. & Mahowald, N. Atlantic Southern Ocean productivity: fertilization from above or below? *Global Biogeochem. Cycles* **21**, GB2006 (2007).

36. Sarmiento, J. L., Slater, R. D., Dunne, J., Gnanadesikan, A. & Hiscock, M. R. Efficiency of small scale carbon mitigation by patch iron fertilization. *Biogeosciences* **7**, 3593–3624 (2010).

37. Brzezinski, M. A., Jones, J. L. & Demarest, M. S. Control of silica production by iron and silicic acid during the Southern Ocean Iron Experiment (SOFeX). *Limnol. Oceanogr.* **50**, 810–824 (2005).

38. Lovenduski, N. S. & Gruber, N. Impact of the Southern Annular Mode on Southern Ocean circulation and biology. *Geophys. Res. Lett.* **32**, L11603 (2005).

39. Cai, W., Cowan, T. & Raupach, M. Positive Indian Ocean Dipole events precondition southeast Australia bushfires. *Geophys. Res. Lett.* **36**, L19710 (2009).

40. Chen, Y. et al. A pan-tropical cascade of fire driven by El Niño/Southern Oscillation. *Nat. Climate Change* **7**, 906–911 (2017).

41. Lim, E.-P. et al. Australian hot and dry extremes induced by weakenings of the stratospheric polar vortex. *Nat. Geosci.* **12**, 896–901 (2019).

42. Cai, W. et al. Increased frequency of extreme Indian Ocean Dipole events due to greenhouse warming. *Nature* **510**, 254–258 (2014).

43. Cropp, R. A. et al. The likelihood of observing dust-stimulated phytoplankton growth in waters proximal to the Australian continent. *J. Mar. Syst.* **117–118**, 43–52 (2013).

44. Hamilton, D. S. et al. Impact of changes to the atmospheric soluble iron deposition flux on ocean biogeochemical cycles in the anthropocene. *Global Biogeochem. Cycles* **34**, e2019GB006448 (2020).

45. Duce, R. et al. Impacts of atmospheric anthropogenic nitrogen on the open ocean. *Science* **320**, 893–897 (2008).

46. Han, Y. et al. Asian inland wildfires driven by glacial-interglacial climate change. *Proc. Natl Acad. Sci. USA* **117**, 5184–5189 (2020).

47. van der Werf, G. R. et al. Global fire emissions estimates during 1997–2016. *Earth Sys. Sci. Data* **9**, 697–720 (2017).

48. Orsi, A. H., Whitworth, T. & Nowlin, W. D. On the meridional extent and fronts of the Antarctic Circumpolar Current. *Deep Sea Res. Part I* **42**, 641–673 (1995).

Article

Methods

Satellite chlorophyll-a observations

The ocean-colour satellite record of chlorophyll a ([Chla]) used in this study is a merged multi-sensor record spanning 22 years and was created by the Ocean Colour Climate Change Initiative (OC-CCI) project[49]. The exact product was the v4.2 weekly chlorophyll-a composite data that includes updates for the latest NASA reprocessing (R2018). The dataset is created by band-shifting and bias-correcting Medium Resolution Imaging Spectrometer (MERIS), Moderate Resolution Imaging Spectroradiometer (MODIS) and Visible Infrared Imaging Radiometer Suite (VIIRS) reflectance data to match Sea-viewing Wide Field-of-view Sensor (SeaWiFS) data, merging the datasets and computing per-pixel uncertainty estimates. The chlorophyll-a products are then calculated from the merged ocean colour remote-sensing reflectance record. More details on data production and access can be found at http://www.esa-oceancolour-cci.org/.

Aerosol reanalysis and deposition

The aerosol optical depth (AOD) and deposition fluxes used in this study are extracted from the Copernicus Atmosphere Monitoring Service (CAMS; http://atmosphere.copernicus.eu), which is a component of the European Earth-observation programme Copernicus (https://www.copernicus.eu/en) produced by the European Centre for Medium-Range Weather Forecasts (ECMWF). CAMS produces global reanalysis datasets of reactive trace gases, greenhouse gases and aerosol concentrations[30]. The CAMS reanalysis consists of three-dimensional time-consistent atmospheric composition fields, including aerosols and chemical species delivered at a frequency of 3–6 h, yet subsampled at a daily frequency for this study. The CAMS aerosol model component is based on the Integrated Forecasting System (IFS) meteorological model[50] and contains 12 prognostic tracers: three size-bins of sea salt, three more for dust, hydrophilic and hydrophobic black carbon (BC) and organic matter (OM), plus sulfate aerosol and a gas-phase sulfur dioxide (SO_2) precursor[30]. CAMS aerosols are assimilated with satellite observations (MODIS)[51] of total AOD at 550 nm. As the aerosol model contains more aerosol components than what can be estimated from AOD satellite observations, the sum of the aerosol species is used as control variable and repartitioned into individual aerosol components according to their fractional contribution to the total aerosol mass[52]. The sources of BC are derived from the Global Fire Assimilation System (GFASv1.2)[53] scaled up with a geographically varying but temporally constant factor[30]. GFASv1.2 estimates near-real-time emissions based on the satellite-observed fire radiative power.

CAMS is a state-of-the-art atmospheric reanalysis that performs well in reproducing observed total AOD and fire-related components such as carbon monoxide (CO) and nitrogen dioxide (NO_2)[54]. The lack of field measurements that disentangle BC AOD from the total AOD, and the difficulty of acquiring field measurements of atmospheric deposition fluxes, particularly for wet deposition in the Southern Hemisphere[55], preclude a direct validation of CAMS performance on these variables. However, given the exceptional emission of BC during the 2019–2020 Australian fire season[56], the uncertainty in the amount of BC in the total AOD estimated from the assimilation is not expected to impact the patterns and variability of BC AOD shown in this study.

Biogeochemical Argo float observations

In situ particulate backscatter (b_{bp}) measurements as a proxy for phytoplankton biomass, taken by autonomous biogeochemical (BGC) Argo profiling floats, were used to corroborate the phytoplankton blooms highlighted by the satellite analyses. [Chla] observed by floats were also provided for comparison. We focus on b_{bp} rather than [Chla] because there are fewer confounding factors for b_{bp} when relating satellite to float data. Satellite [Chla] is based on absorption, whereas float [Chla] is based on fluorescence and affected by non-photochemical quenching and calibration uncertainties. Combining satellite and float b_{bp} observations allowed us to create a satellite climatology of b_{bp} with which to compare the float b_{bp}. The raw float data used here are openly accessible on the Ifremer ftp-server (ftp://ftp.ifremer.fr/ifremer/argo/dac/). Three floats from the Pacific Southern Ocean (float IDs: 5904685, 5904842, 5904843) were selected for the analysis, based on their sampling of the bloom areas identified in the satellite data during 2019–2020 (Fig. 1, float trajectories in Fig. 3). The floats profiled from 2,000 m to the surface every 10 days.

Float and satellite b_{bp} were matched in three steps. First, float b_{bp} at 700 nm wavelength was converted to b_{bp} at 443 nm, the wavelength measured by MODIS Aqua, assuming a spectrally invariant particular backscattering ratio and using the relationship $b_{bp}(443) = b_{bp}(700) \times (\frac{443}{700})^{-\gamma}$, where $\gamma = 0.78$ (refs. [57,58]). Second, from the depth-resolved float b_{bp}, surface b_{bp} estimates at each profile location were then calculated as the median b_{bp} between 0 and 20 m depth. Finally, float surface b_{bp} was calibrated to MODIS Aqua, 8-day, 4 km satellite surface $b_{bp}(443)$ using model II linear regressions (Extended Data Fig. 6). Calibrations were performed individually for each float and were based on the entire b_{bp} dataset gathered during each float's lifetime. To minimize cloud coverage and maximize data availability, satellite values were averaged in time and space in two different ways: 16-day/60×60 km² averages and 24-day/20×20 km² averages. Spatial averages were centred around each profile location. Temporal averages were calculated from two or three consecutive MODIS Aqua 8-day intervals closest to the profile date. The uncertainty introduced by the calibration $b_{bp,cal} = b_{bp} \times a + b$, where a and b are slope and intercept of the regression, was propagated using the regression coefficients' standard deviations: $\sigma b_{bp,cal} = \sqrt{(b_{bp} \times \sigma a)^2 + \sigma b^2}$, where σ denotes the standard deviation.

For each 2019–2020 b_{bp} value, a climatological counterpart was calculated by averaging the respective MODIS Aqua 8-day interval from 2002 to 2018 over a 60×60 km² area centred around the profile location. To reduce the impact of cloud noise on the calibration, b_{bp} match-ups were excluded where the satellite average's relative standard deviation exceeded 10%. The uncertainty of each climatological value is equal to the standard deviation of all b_{bp} values averaged.

Mixed layer depth from Argo floats

Mixed layer depth (MLD) was calculated from the temperature and salinity profiles of Argo floats in the Southern Ocean. Argo floats data were downloaded from https://nrlgodae1.nrlmry.navy.mil, and were filtered by retaining profiles marked with a quality flag of '1' ('good data') or '2' ('probably good data'). The filtered profiles were used to calculate MLD, which is defined as the depth at which the potential density exceeds a near-surface (10 m) reference value by 0.03 kg m⁻³ (refs. [59,60]). The MLD estimates were averaged to obtain monthly resolution in 2° by 2° spatial grids.

Aerosol iron sampling and analysis

The Mount Wellington aerosol time-series sampling station is located at an elevation of 1,271 m above sea level, on the top of Mount Wellington/kunanyi in southern Tasmania, Australia (coordinates: 42.89° S, 147.24° E). Total suspended aerosol particles were collected on acid-washed Whatman 41 cellulose filter paper[61,62] using a high-volume air sampler HiVol 3000 (Ecotech, Rhode Island, USA). Samples used for this study were collected between 17 December 2019 and 11 February 2020 while wildfires were raging in mainland Australia. Samples were collected over 3-day to 2-week periods and stored frozen at the Institute for Marine and Antarctic Studies (Hobart, Tasmania, Australia) prior to analysis. To highlight the impact of the unprecedented fire emissions on aerosol characteristics downwind of the wildfires, aerosol concentrations (total and labile Fe) during the 2019–2020 fire season were compared to measurements made at the same time-series station between October 2016 and December 2019 (mostly from late October to early April annually due to logistic difficulties sampling over winter).

Aerosol Fe concentrations were assessed using a three-step leaching protocol[63]. Sample handling was carried out in an HEPA-filtered laminar flow hood in a positive pressured class 6 clean room, following GEOTRACES procedures[61]. Aerosol samples were successively extracted using an instantaneous flow-through leach of ultra-high purity water, followed by a 1-hour batch leach using a pH 4.7 ammonium acetate buffer solution. Fe concentrations measured in the two leaches were summed to obtain the labile Fe content in aerosols, which is interpreted as an estimate for the bioavailable fraction for marine phytoplankton growth following atmospheric deposition[63,64]. The remaining filter was digested using a mixture of hydrofluoric and nitric acids at 120 °C for 12 h. The sum of the three leaches defines the total Fe concentration in the aerosols. All analyses were undertaken using Sector Field Inductively Coupled Plasma-Mass Spectrometry (SF-ICP-MS, Thermo Fisher Scientific ELEMENT 2; full details in Perron et al. (2020)[63]).

The total Fe concentration measured in aerosols averaged 57.1 ng m^{-3} (median 43.5 ng m^{-3}) before the fire season and increased to 97.2 ng m^{-3} (median 76.6 ng m^{-3}) between 17 December 2019 and 11 February 2020, while wildfires were raging in mainland Australia. The concentration of labile Fe averaged 12.5 ng m^{-3} (median 5.1 ng m^{-3}) over the study period, which exceeds the average labile Fe of 3.5 ng m^{-3} (median 2.7 ng m^{-3}) measured at this sampling site prior to the 2019–2020 fire period while smaller bushfires and anthropogenic emissions prevailed. A t-test (preceded by a variance F-test) was conducted and showed that both total and labile Fe concentrations are statistically different than the historical values ($p < 0.05$ and $p < 0.1$, respectively, in Supplementary Table 1). A greater significance level is acceptable for the labile Fe concentration as this parameter varies highly according to the dominant atmospheric source in aerosols. Indeed, anthropogenic emissions included in aerosols from the time series (prior the fire period) are known to enhance Fe solubility leading to high labile Fe concentration in aerosols.

Chemical tracers were used to differentiate aerosols collected between December 2019 and February 2020 that are only affected by the Australian wildfires and aerosols containing other atmospheric sources. Levoglucosan, a monosaccharide anhydride formed during the pyrolysis of cellulose, served as an intrinsic indicator for biomass burning in aerosols collected during the 2019–2020 Australian wildfire events. Levoglucosan quantitation was carried out by ion chromatography tandem mass spectrometry (IC-MS/MS)[65]. Briefly, a subset of aerosol filter was extracted using 6 ml of deionized water in an ultrasonic bath for 20 min at 20 °C, filtered and analysed using a Thermo Scientific Dionex ICS-5000$^+$ Reagent-Free IC (RFIC) system coupled to a Thermo Scientific TSQ Quantiva triple-stage quadrupole mass spectrometer. As the atmospheric concentration of levoglucosan varies according to the source and location (distance travelled) of the detected fire, this tracer was only used as a qualitative tool in aerosols. In addition, lead and copper were chosen as indicators of anthropogenic emissions in aerosols as the two metals mainly originate from fuel combustion sources. A substantial impact from human-derived emissions on aerosol samples was stated when both enrichment factors (elemental ratio to aluminium compared to the same ratio in the averaged upper continental crust[66]) in lead and copper exceeded the commonly chosen threshold of 10 (ref. [67]). Anthropogenic pollution is known to enhance the fraction of labile Fe in aerosols[68]. Aerosol samples collected during the 2019–2020 peak fire season contained levoglucosan concentrations between 0.26 ng m^{-3} and 283.36 ng m^{-3}, and showed no evidence of anthropogenic contamination.

Atmospheric trajectory analysis

Forward air parcel trajectories were applied to track the transport of aerosols emitted from 2019–2020 Australian wildfires while back trajectories were used to determine the origins of aerosols collected at the aerosol time-series station in Tasmania. These trajectory analyses were performed using the Hybrid Single-Particle Lagrangian Integrated Trajectory model (HYSPLIT)[69]. We used meteorological data acquired from NCEP/NCAR Reanalysis[70] spanning the period from October 2019 to March 2020 (https://www.ready.noaa.gov/archives.php). For the forward trajectories, we analysed some major fire events in southeastern Australia, for example, starting on 26 October 2019 in Gospers Mountain, New South Wales (33° S, 150.4° E), on 26 November 2019 in Shoalhaven, New South Wales (35.5° S, 150.5° E) and on 26 December 2019 in the Stirling Range, Western Australia (34.4° S, 118° E) (https://www.createdigital.org.au/australian-bushfires-a-timeline-of-whats-happened-so-far/ and https://www.nsw.gov.au/nsw-government/projects-and-initiatives/nsw-bushfire-inquiry). The coordinates correspond to the approximate locations of these fires. The model was initiated at 00 UTC and 500 m above ground level for each source region and date to calculate forward trajectories of 168 h (7 days), with a new trajectory launched every 6 h for a duration of 10 days. These parameters are commonly used in previous studies to map the aerosol transport in the atmosphere[71]. In addition, we used these locations to estimate the aerosol emission and transport over the majority of the fire season, that is, trajectories were launched daily and were run from November 2019 to January 2020. The forward trajectories extended mainly around Australia and towards the Pacific Southern Ocean as shown in Extended Data Fig. 2. Air parcel trajectories and wildfire aerosol plumes don't always coincide because of uncertainties in parameters used in the trajectory analysis, for example, the timing and locations of the fires, and the variation in heights that aerosol could reach[72] (Supplementary Discussion).

For the back trajectories, we traced the sources of aerosols collected at the aerosol time-series station in Tasmania. For example, the highest Fe concentration was observed for aerosols collected from 15 January 2020 to 17 January 2020. The model was initiated at 00 UTC 17 January 2020 and at the station location (1,271 m above sea level, 42.89° S, 147.24° E) to calculate back trajectories of 120 h (5 days), with a new trajectory launched every 6 h. Air parcels preferentially originated from the southeastern mainland Australia where wildfires were occurring as shown in Extended Data Fig. 8. Overall, trajectory analysis corroborates the emission and transport of aerosols as seen from the satellite-observed and reanalysed AOD.

Primary production and export production estimates

We estimate the enhancement in marine phytoplankton productivity at the basin scale (20° S–55° S, 120° E–90° W) during the 2019–2020 Australian wildfires shown in Extended Data Fig. 9. Monthly net primary production (NPP) was calculated based on the vertically generalized production model (VGPM)[73], carbon-based production model (CbPM)[74,75], and carbon, absorption, and fluorescence euphotic-resolving model (CAFE)[76] using MODIS satellite observations of monthly chlorophyll-a concentration ([Chla]), photosynthetically available radiation (PAR), MLD, nitracline, inherent optical properties (IOPs), and sea surface temperature (SST) (https://oceancolor.gsfc.nasa.gov/ and http://sites.science.oregonstate.edu/ocean.productivity/index.php). Export production (EP) was determined via multiplying NPP by an export ratio. Three different export ratios[77–79] were separately applied to each NPP model: (1) ef = $0.04756 \times (0.78 - \frac{0.43 \times SST}{30}) \times NPP^{0.307}$; (2) ef= $-0.0081 \times SST + 0.0806 \times \ln([Chla]) + 0.426$; (3) ef = $\frac{8.57}{17.9 + SST}$. Monthly export production was calculated as the mean of the nine estimates. The monthly NPP and EP anomalies were reflected in the differences of monthly NPP and EP during the 2019–2020 wildfire season in comparison to their respective monthly climatologies. We finally integrated the differences from October 2019 to April 2020 to calculate the total additional biological CO$_2$ uptake and export. Uncertainties associated with different algorithms to calculate NPP and export ratio in the ocean are presented in earlier studies[79,80]. We provide the anomalous NPP and EP estimated from each model in the Supplementary Table 2.

Article

Since SST is an important factor in determining the export ratio, we have also applied climatological SST to decipher the contribution of SST anomalies to the enhancement in carbon export (Supplementary Fig. 8). Because of the small and heterogenous SST anomalies, the contribution of SST anomalies to carbon export is negligible compared to the widespread increase in [Chla] or NPP.

Chlorophyll-a anomalies driven by climate variabilities

We evaluated the potential influence of Southern Annular Mode (SAM) and Indian Ocean Dipole (IOD) on the observed anomalies of [Chla] during the 2019–2020 Australian wildfire season. Two linear regression models were developed by using monthly [Chla] anomalies (after removing seasonality) as predictand and using monthly SAM or IOD indices as the predictors for the period 2003–2018 following the method in Lovenduski and Gruber[38]. The monthly SAM[81] and IOD[82] indices were obtained from https://climatedataguide.ucar.edu/climate-data/marshall-southern-annular-mode-sam-index-station-based and https://psl.noaa.gov/gcos_wgsp/Timeseries/DMI/, respectively. The regression models were applied to individual climate indices from December 2019 to February 2020 to predict their impact on monthly [Chla] anomalies. The predicted anomalies are substantially smaller than the observed [Chla] anomalies (Extended Data Fig. 10).

Data availability

The ESA's chlorophyll-a products can be accessed at http://www.esa-oceancolour-cci.org/. Satellite aerosol data are available from the Giovanni online data system (https://giovanni.gsfc.nasa.gov/giovanni/). The Copernicus Atmosphere Monitoring Service (CAMS) aerosol reanalysis datasets can be downloaded from the CAMS Atmosphere Data Store (ADS; https://ads.atmosphere.copernicus.eu/cdsapp#!/dataset/cams-global-reanalysis-eac4?tab=overview). The Argo float data are openly available on the Ifremer ftp-server (ftp://ftp.ifremer.fr/ifremer/argo/dac/). The net primary production estimates are available from the Ocean Productivity website (http://sites.science.oregonstate.edu/ocean.productivity/index.php). Access to datasets analysed in this study is also provided in the Methods section. Datasets generated in this study are provided as Source data and at https://doi.org/10.5281/zenodo.4895657. Source data are provided with this paper.

49. Sathyendranath, S. et al. An ocean-colour time series for use in climate studies: the experience of the Ocean-Colour Climate Change Initiative (OC-CCI). *Sensors* **19**, 4285 (2019).
50. Morcrette, J.-J. et al. Aerosol analysis and forecast in the European Centre for Medium-Range Weather Forecasts Integrated Forecast System: forward modeling. *J. Geophys. Res. Atmospheres* **114**, D06206 (2009).
51. Levy, R. C. et al. Exploring systematic offsets between aerosol products from the two MODIS sensors. *Atmos. Meas. Tech.* **11**, 4073–4092 (2018).
52. Benedetti, A. et al. Aerosol analysis and forecast in the European Centre for Medium-Range Weather Forecasts Integrated Forecast System: 2. Data assimilation. *J. Geophys. Res.* **114**, D13 (2009).
53. Kaiser, J. W. et al. Biomass burning emissions estimated with a global fire assimilation system based on observed fire radiative power. *Biogeosciences* **9**, 527–554 (2012).
54. Y. Bennouna et al. *Validation Report of the CAMS Global Reanalysis of Aerosols and Reactive Gases, Years 2003–2019* (Copernicus Atmosphere Monitoring Service, 2020).
55. Ito, A. et al. Evaluation of aerosol iron solubility over Australian coastal regions based on inverse modeling: implications of bushfires on bioaccessible iron concentrations in the Southern Hemisphere. *Prog. Earth Planet. Sci.* **7**, 42 (2020).
56. Khaykin, S. et al. The 2019/20 Australian wildfires generated a persistent smoke-charged vortex rising up to 35 km altitude. *Commun. Earth Environ.* **1**, 22 (2020).
57. Haëntjens, N., Boss, E. & Talley, L. D. Revisiting Ocean Color algorithms for chlorophyll a and particulate organic carbon in the Southern Ocean using biogeochemical floats. *J. Geophys. Res. Oceans* **122**, 6583–6593 (2017).
58. Boss, E. et al. The characteristics of particulate absorption, scattering and attenuation coefficients in the surface ocean; contribution of the Tara Oceans expedition. *Methods Oceanogr.* **7**, 52–62 (2013).
59. de Boyer Montégut, C., Madec, G., Fischer, A. S., Lazar, A. & Iudicone, D. Mixed layer depth over the global ocean: an examination of profile data and a profile-based climatology. *J. Geophys. Res. Oceans* **109**, C12003 (2004).
60. Dong, S., Sprintall, J., Gille, S. T. & Talley, L. Southern Ocean mixed-layer depth from Argo float profiles. *J. Geophys. Res. Oceans* **113**, C06013 (2008).
61. Cutter, G. A. et al. Sampling and Sample-handling Protocols for GEOTRACES Cruises, version 3.0 (2017).
62. Morton, P. L. et al. Methods for the sampling and analysis of marine aerosols: results from the 2008 GEOTRACES aerosol intercalibration experiment. *Limnol. Oceanogr. Methods* **11**, 62–78 (2013).
63. Perron, M. M. G. et al. Assessment of leaching protocols to determine the solubility of trace metals in aerosols. *Talanta* **208**, 120377 (2020).
64. Shelley, R. U., Landing, W. M., Ussher, S. J., Planquette, H. & Sarthou, G. Regional trends in the fractional solubility of Fe and other metals from North Atlantic aerosols (GEOTRACES cruises GA01 and GA03) following a two-stage leach. *Biogeosciences* **15**, 2271–2288 (2018).
65. Sanz Rodriguez, E. et al. Analysis of levoglucosan and its isomers in atmospheric samples by ion chromatography with electrospray lithium cationisation—triple quadrupole tandem mass spectrometry. *J. Chromatogr. A* **1610**, 460557 (2020).
66. McLennan, S. M. Relationships between the trace element composition of sedimentary rocks and upper continental crust. *Geochem. Geophys. Geosyst.* **2**, 1201 (2001).
67. Shelley, R. U. et al. Quantification of trace element atmospheric deposition fluxes to the Atlantic Ocean (>40°N; GEOVIDE, GEOTRACES GA01) during spring 2014. *Deep Sea Res. Part I* **119**, 34–49 (2017).
68. Sholkovitz, E. R., Sedwick, P. N., Church, T. M., Baker, A. R. & Powell, C. F. Fractional solubility of aerosol iron: synthesis of a global-scale data set. *Geochim. Cosmochim. Acta* **89**, 173–189 (2012).
69. Stein, A. F. et al. NOAA's HYSPLIT atmospheric transport and dispersion modeling system. *Bull. Am. Meteorol. Soc.* **96**, 2059–2077 (2016).
70. Kalnay, E. et al. The NCEP/NCAR 40-year reanalysis project. *Bull. Am. Meteorol. Soc.* **77**, 437–471 (1996).
71. Tatlhego, M., Bhattachan, A., Okin, G. S. & D'Odorico, P. Mapping areas of the Southern Ocean where productivity likely depends on dust-delivered Iron. *J. Geophys. Res. Atmospheres* **125**, e2019JD030926 (2020).
72. Stein, A. F., Rolph, G. D., Draxler, R. R., Stunder, B. & Ruminski, M. Verification of the NOAA smoke forecasting system: model sensitivity to the injection height. *Weather Forecast.* **24**, 379–394 (2009).
73. Behrenfeld, M. J. & Falkowski, P. G. Photosynthetic rates derived from satellite-based chlorophyll concentration. *Limnol. Oceanogr.* **42**, 1–20 (1997).
74. Behrenfeld, M. J., Boss, E., Siegel, D. A. & Shea, D. M. Carbon-based ocean productivity and phytoplankton physiology from space. *Global Biogeochem. Cycles* **19**, GB1006 (2005).
75. Westberry, T., Behrenfeld, M. J., Siegel, D. A. & Boss, E. Carbon-based primary productivity modeling with vertically resolved photoacclimation. *Global Biogeochem. Cycles* **22**, GB2024 (2008).
76. Silsbe, G. M., Behrenfeld, M. J., Halsey, K. H., Milligan, A. J. & Westberry, T. K. The CAFE model: a net production model for global ocean phytoplankton. *Global Biogeochem. Cycles* **30**, 1756–1777 (2016).
77. Laws, E. A., D'Sa, E. & Naik, P. Simple equations to estimate ratios of new or export production to total production from satellite-derived estimates of sea surface temperature and primary production. *Limnol. Oceanogr. Methods* **9**, 593–601 (2011).
78. Dunne, J. P., Armstrong, R. A., Gnanadesikan, A. & Sarmiento, J. L. Empirical and mechanistic models for the particle export ratio. *Global Biogeochem. Cycles* **19**, GB4026 (2005).
79. Li, Z. & Cassar, N. Satellite estimates of net community production based on O_2/Ar observations and comparison to other estimates. *Global Biogeochem. Cycles* **30**, 735–752 (2016).
80. Siegel, D. A. et al. Global assessment of ocean carbon export by combining satellite observations and food-web models. *Global Biogeochem. Cycles* **28**, 181–196 (2014).
81. Marshall, G. J. Trends in the Southern Annular Mode from observations and reanalyses. *J. Climate* **16**, 4134–4143 (2003).
82. Saji, N. H. & Yamagata, T. Possible impacts of Indian Ocean Dipole mode events on global climate. *Climate Res.* **25**, 151–169 (2003).

Extended Data Fig. 1 | Emission and deposition of aerosols and response of phytoplankton. a, Monthly aerosol optical depth (AOD) at 550 nm observed by MODIS satellite during the 2019–2020 Australian wildfires from November 2019 to February 2020. **b**, Monthly chlorophyll-a absolute anomaly. **c**, Monthly cumulative black carbon aerosol deposition. Contour lines indicate the monthly maximum black carbon AOD (black = 0.05, grey = 0.1, light-grey = 0.15). All: Subtropical, Subantarctic and Polar Fronts are indicated with a dotted, a dashed and a solid black line, respectively[48].
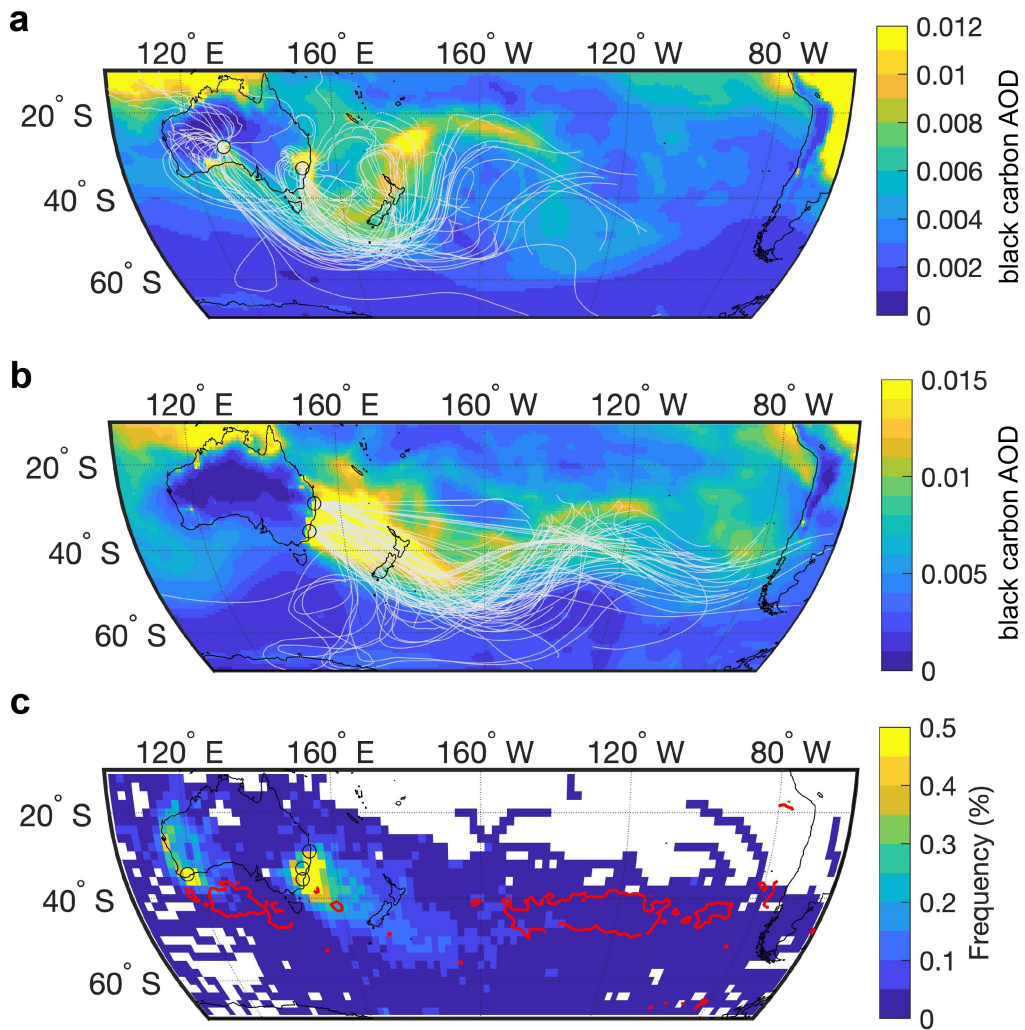
Extended Data Fig. 2 | Forward trajectories tracking the emission and transport of aerosols from major fire events during the 2019–2020 Australian wildfires. a, Seven-day trajectories (grey lines) launched every 6 h and originated from wildfires during the period of 26 October to 4 November 2019 and black carbon AOD from the same period shown as the background map. The trajectory origins are depicted by black circles. The distribution of trajectories generally follows the black AOD pattern. **b**, Seven-day trajectories (grey lines) originated from wildfires during the period of 26 November to 5 December 2019. **c**, The spatial distribution of 7-day trajectory endpoints frequencies in 2° by 2° grid over the period of November 2019 to January 2020. The trajectory origins are depicted by black circles to represent the major fires' locations. The 7-day air parcel forward trajectories were launched daily. The red contours depict regions where [Chla] more than doubled during the same period compared with their climatologies. The large [Chla] anomalies generally occurred in regions over which the trajectories passed.
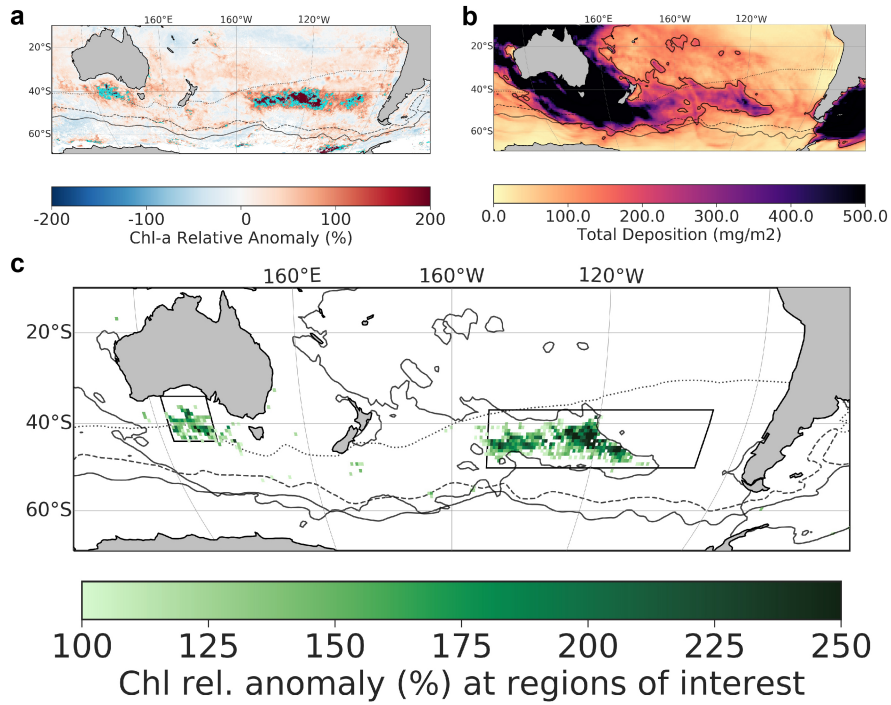
Extended Data Fig. 3 | Identification of regions of interest with potential aerosol fertilization. a, Austral summer (DJF) 2019–2020 averaged chlorophyll-a relative anomaly map with cyan contour lines indicating where the anomaly is equal to 100%. **b**, Austral summer (DJF) 2019–2020 cumulative deposition of dust and black-carbon with black contour line indicating where deposition is equal to 150 mg m^{-2}. **c**, Pixels where both [Chla] relative anomaly exceeds 100% and cumulative deposition exceeds 150 mg m^{-2} are marked in green. Black boxes indicate the South of Australia and Pacific Southern Ocean regions defined in this study. All: Subtropical, Subantarctic and Polar Fronts are indicated with a dotted, a dashed and a solid black line, respectively.
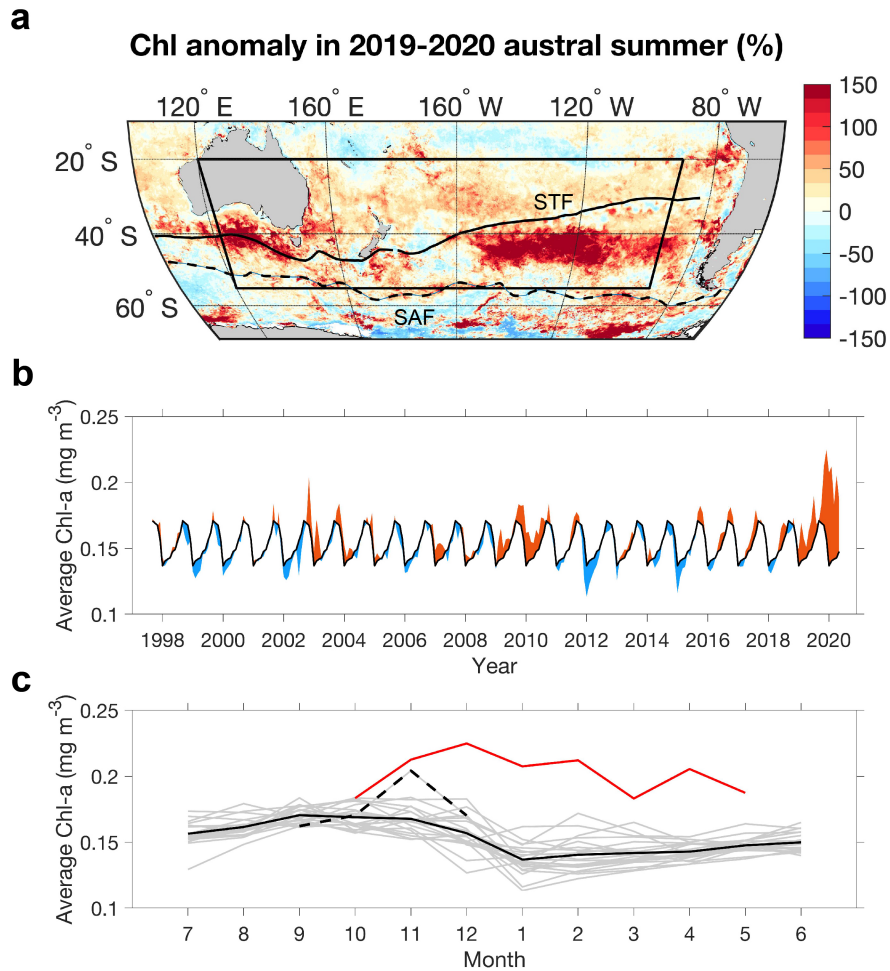
Extended Data Fig. 4 | Large chlorophyll-a ([Chla]) anomaly in a big box region of the South Pacific and Southern Ocean during 2019–2020 Australian wildfires. a, [Chla] anomaly map from December 2019 to February 2020 in comparison to their climatologies. A large portion of the ocean basin (solid black box) was selected to calculate [Chla] time-series. STF, Subtropical Front; SAF, Subantarctic Front. **b**, Time-series of average [Chla] in the selected box region. Monthly climatological values shown in solid black line. Red and blue areas denote monthly data higher or lower than climatological values, respectively. **c**, Monthly average [Chla] in individual years in the selected box region. Grey lines, historical years; solid black line, monthly climatologies; dashed black line, 2002 Australian wildfire season; red line, 2019–2020 Australian wildfire season.
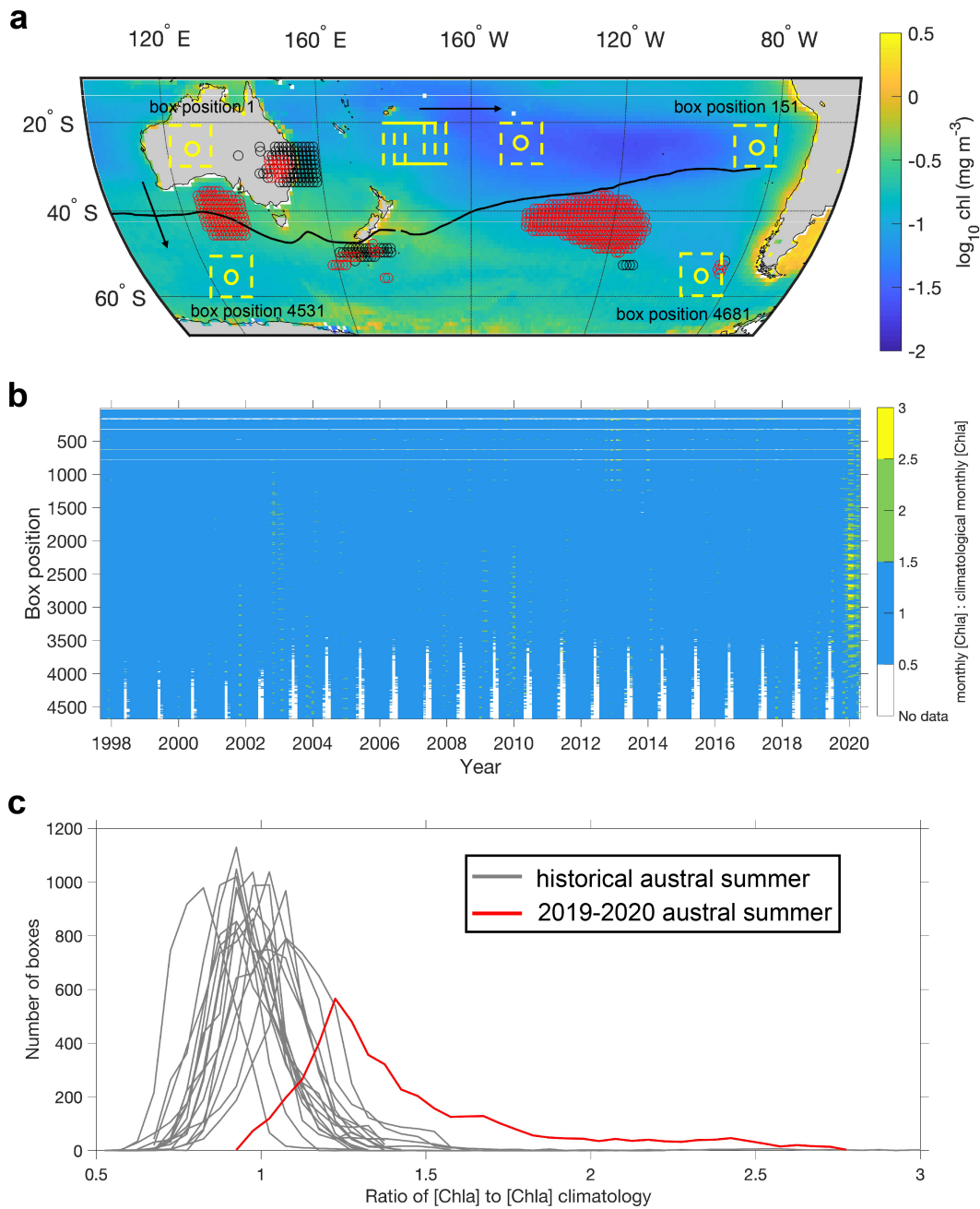
Extended Data Fig. 5 | Large chlorophyll-a ([Chla]) anomaly in numerous small box regions during 2019–2020 Australian wildfires. a, [Chla] time-series was calculated in 4,681 of 10° by 10° boxes from 1997 to 2020 in the broad South Pacific and Southern Ocean (20° S–60° S; 120° E–80° W). Yellow circles and yellow dashed boxes are examples to show the center and coverage of each box region. Box moves by 1° eastward and southward sequentially illustrated by the black arrows. Box position 1, 151, 4,531 and 4,681 denoting the edge of the study region are shown as examples on the map of annual [Chla] climatology. The ratio of monthly [Chla] to its monthly climatology is calculated for each 10° by 10° box starting from October 1997 to May 2020. Black circles: centre locations of 10° by 10° boxes where $\frac{monthly[Chla]}{[Chla]climatology} > 2.5$ before the 2019–2020 wildfires (from October 1997 to August 2019); red circles: centre locations of 10° by 10° boxes where $\frac{monthly[Chla]}{[Chla]climatology} > 2.5$ during or after the 2019–2020 wildfires (from September 2019 to May 2020). Historically, regions with a large anomaly (black circles) are mostly located in coastal waters (for example, east coast of Australia). In contrast, during the 2019–2020 Australian wildfires (red circles), large areas of the open ocean show a high [Chla] anomaly (for example, south of Australia and Pacific sector of the Southern Ocean). Oceanic [Chla] anomalies of this magnitude are unprecedented in the historical record. Some of the black and red circles are on land because a fraction of the 10° by 10° box around these circles covers the ocean. **b**, Ratio of monthly [Chla] to its corresponding monthly climatologies for each box region from 1997 to 2020. **c**, Frequency distributions of the monthly [Chla] to monthly climatology ratios over the historical and 2019–2020 austral summers.
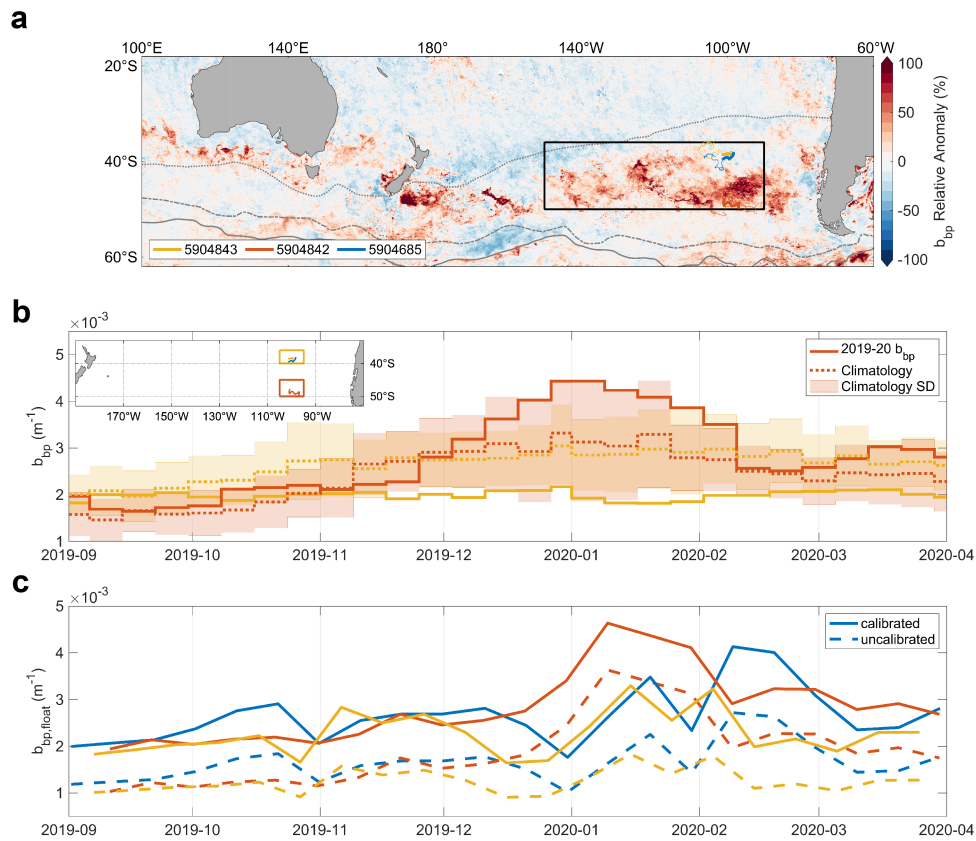
Extended Data Fig. 6 | Maps of b_{bp} anomalies and comparison between calibrated and uncalibrated BGC Argo in situ b_{bp} measurements. a, Satellite backscatter b_{bp} relative anomaly for the 2019–2020 austral summer. Bloom region and BGC-Argo float trajectories superimposed on the map. Float positions from September 2019 through March 2020 highlighted. The southern float (red) was in a biologically more active region of the bloom than the two northern floats (blue and yellow). This corroborates the stronger bloom signal shown by the southern float. Dotted, dot-dashed, and solid lines in **a** represent the climatological positions of the Subtropical Front, Subantarctic Front and Polar Front, respectively[48]. **b**, Satellite b_{bp} averaged over two sub-regions encompassing the float paths. The solid lines are 2019–2020 observations and the dotted lines with coloured standard deviation envelopes are the climatology. This analysis corroborates the stronger bloom signal shown by the southern float compared with the two northern floats.
c, Comparison between uncalibrated (dashed lines) and calibrated (solid lines) in situ b_{bp} measured by the three BGC-Argo floats. Surface b_{bp} estimates were calculated as the median b_{bp} between 0 and 20 m depth and then calibrated using a linear regression (see Methods for details). The calibration was applied to allow for comparison between float b_{bp} and the satellite-based climatology. The general trend of the float signal is not altered by the calibration.
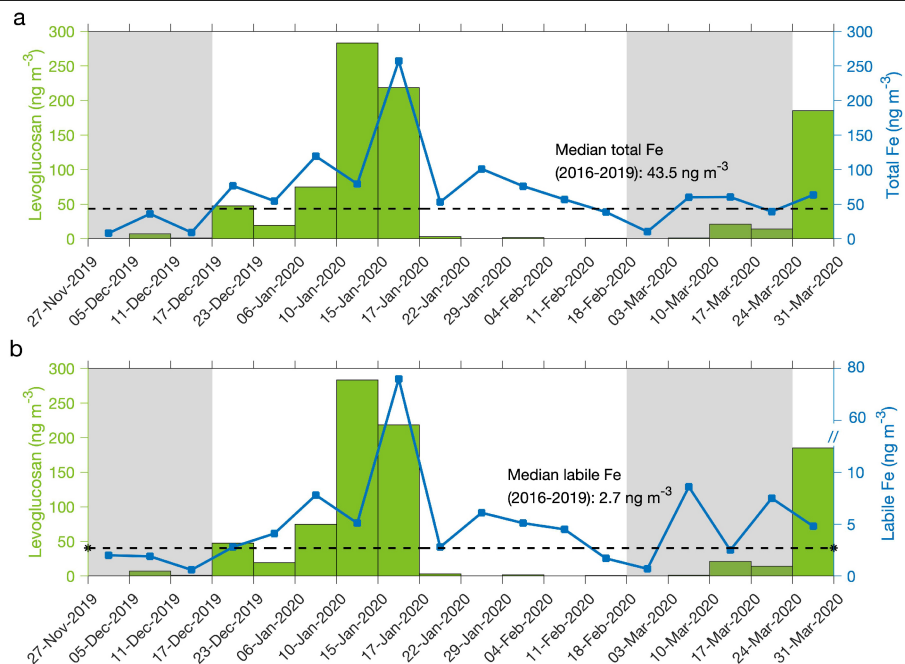
Extended Data Fig. 7 | Iron (Fe) concentration and origin of aerosols collected at an aerosol time-series sampling station in Tasmania during the 2019–2020 Australian wildfires. a, Total Fe concentration (blue line) during the 2019–2020 Australian wildfire season is compared with the historical median value from 2016–2019 (dashed black line). High levoglucosan concentration (green bar) indicates wildfire-derived aerosols. Grey shaded areas represent samples influenced by anthropogenic sources. See Methods for the use of tracers to track the sources of aerosols. **b**, Labile Fe concentration (blue line) during the 2019–2020 Australian wildfire season is compared with the historical median value from 2016–2019 (dashed black line). The aerosols with high Fe content collected around 15 January 2020 are likely to have originated from wildfires, indicated by the high concentration of levoglucosan concentrations and low concentration of anthropogenic tracers.
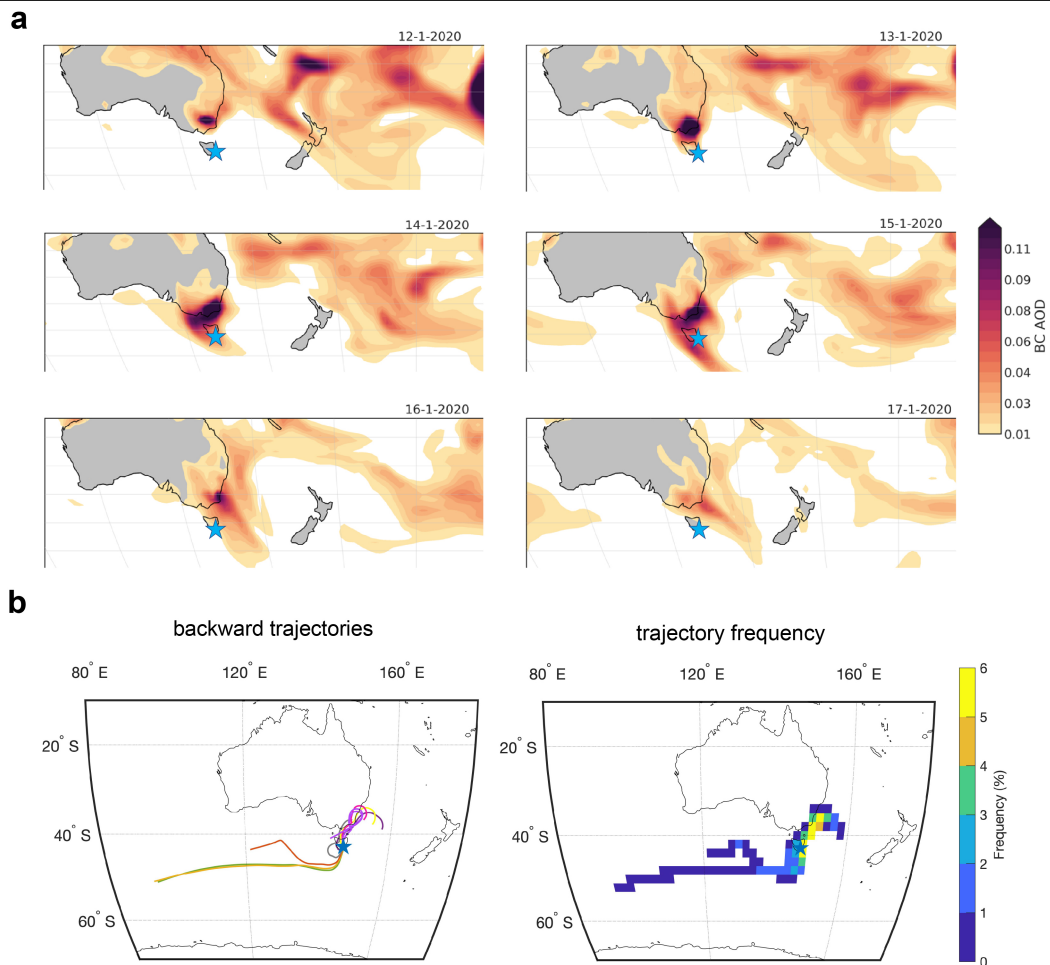
Extended Data Fig. 8 | Tracking the origins of aerosols with high iron content collected at an aerosol time-series sampling station in Tasmania during 15–17 January 2020. a, High black carbon AOD plume passing the sampling station (cyan star). **b**, Five-day backward trajectories were launched every 6 h from the sampling station (cyan star) during 15–17 January 2020. Both the distribution of trajectories and the frequency of trajectories' endpoints confirm that the majority of the aerosols came from southeastern Australia where wildfires were raging.
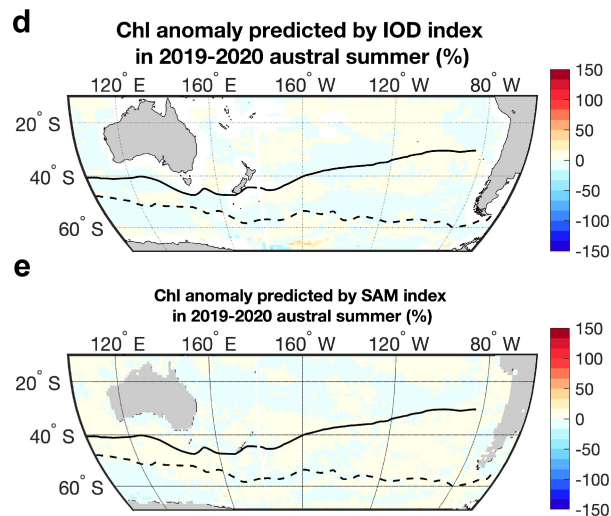
a

b
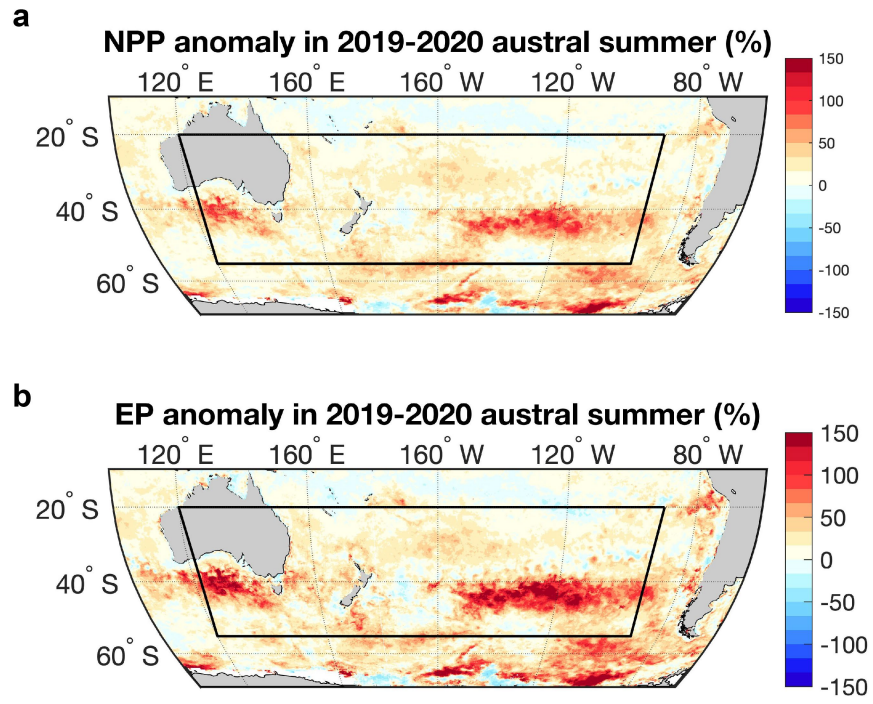
Extended Data Fig. 9 | Anomalies in marine phytoplankton productivity during 2019–2020 Australian wildfires. a, b, Net primary production (NPP) (**a**) and export production (EP) (**b**) anomalies in 2019–2020 austral summer relative to their climatologies. Black boxes denote the basin-scale regions (20° S–55° S, 120° E–90° W) used to estimate changes in marine production during the 2019–2020 Australian wildfires.
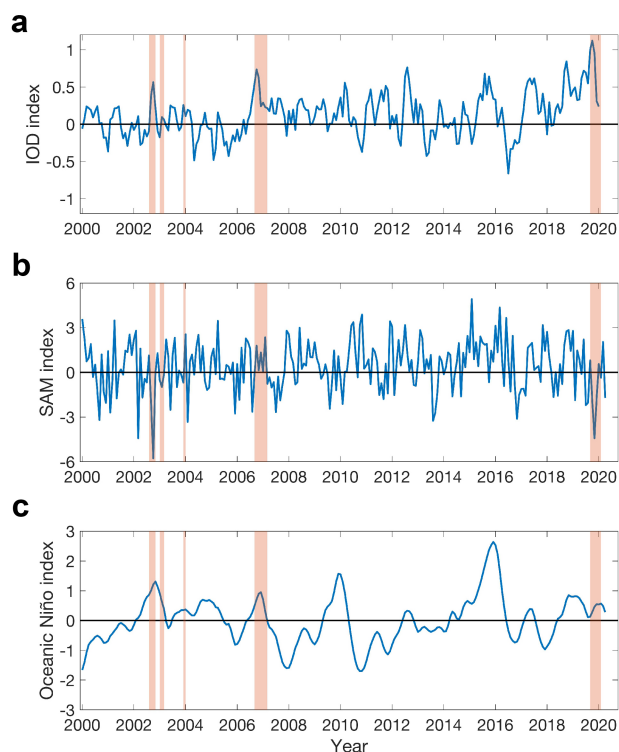
Extended Data Fig. 10 | Relations of large-scale climate patterns to the occurrence of wildfires and to chlorophyll a distribution. a–c, Time-series of climate indices Indian Ocean Dipole (IOD) (**a**), Southern Annular Mode (SAM) (**b**) and Oceanic Niño Index (**c**). Historical Australian mega-wildfire periods shaded in orange (>1 million hectares of land burned). **d**, [Chla] anomaly predicted by IOD index during the 2019–2020 Australian wildfires. **e**, [Chla] anomaly predicted by SAM index during the 2019–2020 Australian wildfires. The [Chla] anomaly potentially induced by the climate patterns are substantially smaller than the observed [Chla] anomaly (Fig. 1d).